

Theoretical Study for Safe and Efficient Energy Transfer to Deeply Implanted Devices Using Ultrasound

Benjamin Cotté, Cyril Lafon, Catherine Dehollain, and Jean-Yves Chapelon

Abstract—The goal of this paper is to prove that a safe and efficient energy transfer is possible between an external transducer located on the patient's skin and a device deeply implanted in the abdomen. An ultrasound propagation model based on the Rayleigh–Sommerfeld diffraction integral is coupled with the data from the Visible Human Project to account for the geometry of the organs in the body. The model is able to predict the amount of acoustic power received by the device for different acoustic paths. The acoustic model is validated by comparison with measurements in water and in heterogeneous liquid phantoms. Care is taken to minimize adverse bioeffects—mainly temperature rise and cavitation in tissues. Simulations based on the bio-heat transfer equation are performed to check that thermal effects are indeed small.

I. INTRODUCTION

THE technology evolution in the last decades, and particularly the advancements in microelectronics, has promoted the use of implantable medical devices for both diagnostic and therapeutic purposes. Examples of devices designed to be implanted in the body for monitoring purposes are glucose biosensors [1], pH sensors [2], pressure sensors [3], or impedance sensors for chronic heart failure monitoring [4]. Other devices are designed for therapeutic applications, such as pacemakers, defibrillators, insulin pumps, or micro-oxygen generators used to enhance the efficacy of tumor treatment by radiation therapy [5]. In spite of these advances, design issues for implanted medical devices remain numerous, the most important challenges being miniaturization and low power consumption.

All medical devices require energy sources to carry out their functions, and different methods for powering them have been proposed. First, different methods have been introduced in recent years to produce electrical power from other energy sources present in the environment or in the human body; they are reviewed by Lueke and Moussa [6]. These self-powered energy harvesting devices can convert electricity either from ambient light (using photovoltaic cells), ambient thermal energy, vibration energy (using,

for instance, piezoelectric generators), or using chemistry-based techniques (such as fuel cells). These techniques typically generate an average power of less than 1 mW; thus, they are still limited to ultra-low-power applications. A second class of methods supplies power wirelessly through the skin from an external energy source. This transcutaneous energy transfer (TET) can be done with electromagnetic or ultrasonic waves. Electromagnetic devices typically use a pair of flat spiral coils facing each other, with one external transmitting coil and one intrabody receiving coil. They can generate average power of up to 20 W but are limited to small distances, typically 1 or 2 cm [7]–[9]. Also, it is becoming more difficult to ensure radio communication with a high immunity to external radiators [10].

This paper considers acoustic powering of implantable medical devices, a topic that has received growing interest in the past years [11]–[14], because this technique has several advantages compared with RF techniques. Ultrasonic TET devices have a better efficiency than electromagnetic TET devices when the distance between source and receiver is greater than approximately 2 cm [9]. Ultrasonic TET devices are compact and immune to electromagnetic radiation [10].

In this study, our goal is to prove that energy can be transferred efficiently and safely from an emitting transducer, located externally on the patient's skin, to a receiving transducer deeply implanted in the body (typically 10 cm or more from the external transducer). The propagation distance was smaller in the work of Ozeri *et al.* [14], who considered ultrasonic transcutaneous energy transfer for devices implanted up to 5 cm deep. Based on a model for ultrasound propagation in a realistic body geometry, we propose suitable acoustic paths between the external transducer and the implanted device, to maximize the energy transfer and to limit adverse bioeffects, especially temperature rise and cavitation in tissues. We chose an implantation site in the abdomen, which would be suitable for empowering, as examples, sensors monitoring pH at the gastro-esophageal junction or pressure at the hepatic portal vein, with typical power consumption of a few tens to a few hundreds of milliwatts [10].

The proposed acoustic model is based on the Rayleigh–Sommerfeld diffraction integral, and is coupled with the data from the Visible Human Project (VHP) to account for the geometry of the organs in the body. This model is able to predict the amount of acoustic power that can be sent to a given device position while minimizing adverse

Manuscript received January 13, 2012; accepted May 24, 2012. The research leading to these results has received funding from the European Community's Seventh Framework Programme (FP7/2007-2013) under grant agreement number 224009.

B. Cotté, C. Lafon, and J.-Y. Chapelon are with the Institut National de la Santé et de la Recherche Médicale (INSERM), U556, Lyon, France, and Université de Lyon, Lyon, France (e-mail: cyril.lafon@inserm.fr).

C. Dehollain is with the RF IC Group at the Ecole Polytechnique Fédérale de Lausanne (EPFL), Lausanne, Switzerland.

DOI <http://dx.doi.org/10.1109/TUFFC.2012.2373>

bioeffects. A 64-element array working at a center frequency of 1 MHz is considered in this paper. This choice of ultrasound frequency is the result of a compromise. At higher frequencies, penetration depth in tissues is reduced and thermal effects are more important. At lower frequencies, beamforming techniques are less efficient and the likelihood of cavitation is increased. It can be mentioned that this type of model could also be used in other applications, such as hyperthermia and ultrasound surgery (thermal ablation by ultrasound), but other uses are outside the scope of this paper.

The acoustic model coupled with the VHP data is first described in Section II, along with the thermal model used to predict the temperature rise in tissues resulting from ultrasound propagation. The acoustic model is then validated against *in vitro* measurements in Section III. Model results for different acoustic paths are detailed in Section IV and discussed in Section V.

II. MODELING OF ULTRASOUND PROPAGATION AND TEMPERATURE RISE IN TISSUE USING THE VISIBLE HUMAN PROJECT DATA

A. Selection of Acoustic Paths Using the Visible Human Project Data

To transfer energy to a device located in the abdomen, suitable acoustic paths must be found that avoid the bones, the lungs, and hollow structures of the digestive system. Two main positions of the external transducer, located on the patient's skin, can be envisaged. In the first position, the transducer is in front of the intercostal space (between ribs 4 and 5), and in the second position, it is located below the ribs. The corresponding acoustic paths will be referred to as the intercostal and subcostal paths hereafter.

Using the inner organs segmented data of the Visible Human Male provided by VOXEL-MAN (Hamburg, Germany), the tissue layers along each acoustic path can be identified and visualized. Frozen computed tomography (CT) scans are plotted in Fig. 1 for the two positions of the transducer considered in this paper. The transducer array that is used in the pressure field measurements in Section III and in the simulations in Section IV is shown in gray. The acoustic axis of the array is represented as a white dashed line and the target point as a white dot. Also, some of the tissue types are indicated in these figures using the abbreviations given in Table I. The target point corresponding to one point on the device surface is located between the heart, the liver and the stomach. As can be seen in Fig. 1, the array has been tilted so that it is in contact with the skin. For the intercostal path, the target point is away from the acoustic axis, with a focal point at $x_F = 30$ mm and $z_F = 150$ mm, where the axes are defined as in Fig. 2. For the subcostal path, the target point is at 160 mm from the array on the acoustic axis z .

The segmented data are originally given in a Cartesian mesh of spacing 1 mm; a tissue layer is associated with

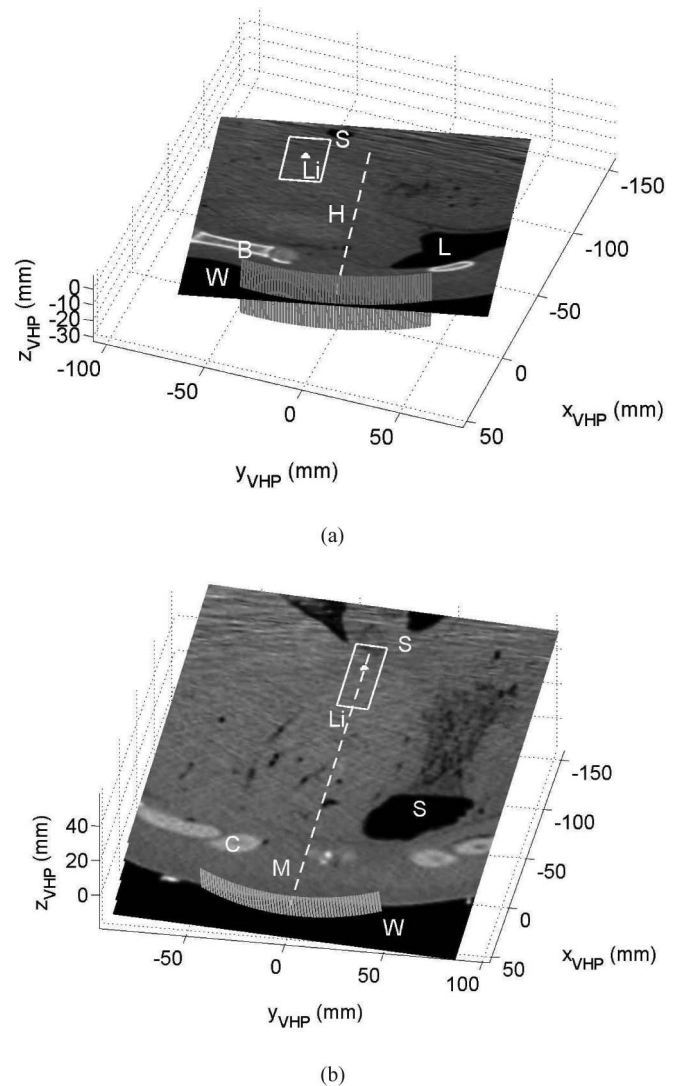


Fig. 1. Frozen computed tomography scans for (a) the intercostal path and (b) the subcostal path. The white dashed line corresponds to the acoustic axis of the array, the white dot to the target point, and the white solid lines to the limits of the computation domain for the simulations presented in Section IV.

each point of the mesh. A computational grid is then defined that contains the points at which the acoustic field should be calculated, and the tissue layer associated with each point of this grid is obtained using interpolation to the nearest point. In Fig. 1, the white lines correspond to the limits of the computation domain for the simulations presented in Section IV-B.

Following Pichardo and Hynynen [15], the grid points are split into two categories: soft tissue voxels and blocking voxels. Blocking voxels correspond to tissue layers that greatly attenuate ultrasound waves, and thus prevent ultrasound to propagate to the target point; bones, lungs, and stomach are considered as blocking voxels. Soft-tissue voxels, on the contrary, correspond to tissue layers whose properties in terms of density and sound speed are close to the properties of water, enabling ultrasound waves to propagate through them.

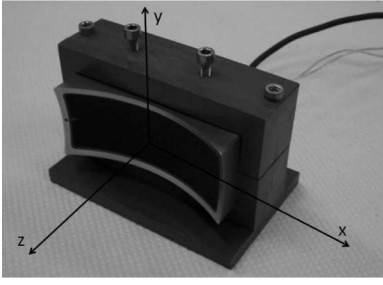


Fig. 2. Photograph of the 64-element spherical linear array considered in this paper and definition of the axes x , y , and z .

B. Acoustic Model Based on the Rayleigh–Sommerfeld Integral

The acoustic model is based on an approximate theory for the acoustic radiation of focused transducers in a homogeneous and nonabsorbing medium [16]. Continuous-wave signals are considered. The complex velocity potential ψ is calculated by the Rayleigh–Sommerfeld diffraction integral:

$$\psi(r) = \frac{1}{2\pi} \iint_S V_n \frac{e^{-jk_0 r}}{r} dS, \quad (1)$$

where $k_0 = 2\pi f_c / c_0$ is the acoustic wave number, f_c is the acoustic frequency, c_0 is the speed of sound in the medium, r is the distance between an element dS of the transducer and the field point, and V_n the normal velocity on dS . Eq. (1) can be evaluated numerically by dividing the transducer surface into M elements small enough that they can be treated as point sources, thus yielding [17], [18]

$$\psi(r) = \frac{1}{2\pi} \sum_{m=1}^M V_{n,m} \frac{e^{-jk_0 r_m}}{r_m} \Delta S_m. \quad (2)$$

In the calculations, the dimensions of the small elements are chosen to be smaller than a fifth of the acoustic wavelength. Then, the acoustic pressure P can be deduced using:

$$P(r) = \rho_0 \frac{\partial \psi(M, t)}{\partial t} = j2\pi f_c \rho_0 \psi(r), \quad (3)$$

where ρ_0 is the medium density, and using the $e^{j\omega t}$ convention.

In a medium with N tissue layers, where ρ_i , c_i , and α_i are respectively the density, sound speed, and attenuation coefficient of layer i , sound waves can be reflected and refracted because of the difference between the impedances $Z_i = \rho_i c_i$ of the different layers. It is possible to use a ray model to calculate the reflected and refracted fields (secondary source model), as was done, for instance, by Fan and Hynynen [17] and Moros *et al.* [18]. This method is suitable when a limited number of tissue layers are considered (typically $N = 2$), but cannot be followed when a realistic geometry needs to be considered, such as the one shown in Fig. 1. The approach chosen in this study is to account for the ultrasound attenuation in the different tissue layers, and to neglect the effects of refraction and reflection. This approach is valid when the impedance differences are sufficiently small, as is typically true for soft tissue layers. It will be seen in Section II-D that the impedances Z_i of the soft tissues are in the range of 1.4 to 1.8 MRayl. The other types of tissue, such as bones and lungs, are considered as blocking voxels, as explained in Section II-A. Thus, following Pichardo and Hynynen [15], any path between an element ΔS_m of the array and the field point that crosses a blocking tissue is not considered in the summation of (2).

The attenuation can be taken into account by replacing the real wave number k_0 by the complex wave number $k = k_0 - j\alpha$, where α is the pressure amplitude attenuation coefficient of the medium [18]. Thus, (2) becomes

$$\psi(r) = \frac{1}{2\pi} \sum_{m=1}^M V_{n,m} e^{-\sum_{i=1}^N \alpha_i r_{m,i}} \frac{e^{-jk_0 r_m}}{r_m} \Delta S_m, \quad (4)$$

with $r_m = \sum_{i=1}^N r_{m,i}$. The model will be compared against measurements in water and in heterogeneous media made with liquid phantoms in Section III.

C. Thermal Model Based on the Bio-Heat Transfer Equation

The thermal model is based on the bio-heat transfer equation (BHTE) given by [19]

TABLE I. PARAMETERS OF THE TISSUE LAYERS AT TEMPERATURE T AND AT A FREQUENCY OF 1 MHz.

Tissue type	Abbreviation	c (m/s)	α (dB/cm)	ρ (kg/m ³)	C_p (J/kg per K)	K (W/m per K)	m_b (kg/m ³ per s)	T (°C)
Cartilage	C	1600	4.0	1100	—	—	—	37
Fat	F	1450	0.8	950	3100	0.270	0.5	37
Liver	Li	1595	0.5	1060	3600	0.524	18.7	37
Muscle (cardiac)	H	1570	0.5	1060	3720	0.537	15.0	37
Muscle (skeletal)	M	1580	0.7	1050	3465	0.498	0.7	37
Skin	—	1615	3.5	1090	—	—	—	37
Bone	B	—	—	—	—	—	—	—
Lung	L	—	—	—	—	—	—	—
Stomach	S	—	—	1050	3550	0.525	7.4	37
Blood	—	1580	0.2	1060	3720	—	—	37
Water	W	1480	2.2×10^{-3}	1000	—	—	—	20

$$\rho C_p \frac{\partial T}{\partial t} = (\nabla \cdot K) \nabla T + m_b C_{pb} (T_a - T) + Q, \quad (5)$$

where T is the tissue temperature and T_a is the arterial temperature, C_p is the specific heat and C_{pb} is the specific heat of blood, K is the thermal conductivity of tissue, and m_b is the local perfusion rate. The term on the left-hand side of (5) corresponds to the variation in internal energy per unit volume, the first term on the right-hand side to thermal conduction, and the second term to the phenomenon of blood perfusion. Q is the local deposited heat per unit volume [17]: $Q = 2\beta\alpha I_a = \beta\alpha |P|^2/\rho c$. We assume $\beta = 1$, which means that attenuation is only due to absorption. This assumption leads to an overestimation of the actual temperature rise, and corresponds to a worst-case scenario from a safety point of view.

Eq. (5) is solved using finite-difference time-domain techniques described in [20], as was done in [21]. The temperature is set to a constant value (37°C) on the boundaries. It is thus important to consider a large enough domain, as will be seen in Section IV-C, to avoid any artificial cooling effect from the boundaries of the computation domain.

D. Acoustic and Thermal Parameters of the Tissue Layers

For the configurations studied in this paper, six tissue layers are present in the VHP data which are considered as soft tissue voxels. These tissue types are listed in Table I, along with their characteristic properties. The attenuation coefficient α varies greatly among tissue layers, between 0.5 and 4.0 dB/cm at 1 MHz, with the highest values for skin and cartilage tissue. Properties for blood and water are also given; the coupling medium between the transducer surface and the skin is treated as water. Finally, the thermal properties are listed in Table I only for tissue layers present in the temperature rise calculations performed in Section IV-C. The values of these properties are taken from [22] and [23], and completed by values from [24] for fat and skin and from [25] for cartilage. In Table I, abbreviations used throughout the paper for the different tissue layers are also defined.

III. EXPERIMENTAL VALIDATION OF THE ACOUSTIC MODEL

In this section, the acoustic model described in Section II-B is validated by comparison with pressure field measurements. The first set of measurements, presented in Section III-C, takes place in water and shows the beam-forming abilities of the array. In the second set of measurements, described in Section III-D, a heterogeneous medium is obtained by placing flasks filled with three different liquid phantoms in water to test the influence of refraction effects. Before comparing the model to these measurements, Section III-A describes how the acoustic properties of the liquid phantoms are measured, and the setup for the pressure field measurements is presented in Section III-B.

A. Characterization of the Acoustic Properties of the Liquid Phantoms

In Section III-D, the following liquid phantoms are considered:

- castor oil (La Grande Pharmacie Lyonnaise, Lyon, France);
- rapeseed oil (from the local grocery store);
- diethylene glycol (H26456, Sigma-Aldrich, St. Quentin Fallavier, France).

The liquid phantoms are contained in three 250-mL flasks (no. 353024, Becton Dickinson France SAS, Le Pont de Claix, France) whose walls were removed on each side to obtain an acoustic window of size 9×4 cm. A thin film of polyurethane (transducer cover CIV-Flex ref. 610542, CIVCO, Euro Diffusion Médicale, Sarcelles, France) was placed to keep the liquid in the flask without attenuating the ultrasonic waves passing through the film. To obtain the sound speed and attenuation coefficient of these liquid phantoms, we used the through-transmission water-substitution method described by Kossoff *et al.* [26]. A schematic diagram of the experiment is shown in Fig. 3. Two 1-in (2.54-cm) plane transducers of center frequency 1 MHz (A302S and V302, Olympus Panametrics-NDT, Rungis, France) were used for this characterization experiment, which took place in a tank filled with degassed and deionized water at a temperature of 22°C. Narrowband excitation signals centered at 1 MHz were chosen for the measurements presented here.

The travel times of the echoes reflected back from the liquid phantoms are obtained with TR_1 in emission to deduce the distance d_1 , and with TR_2 in emission to deduce the distance d_2 . The distance between the transducers L is deduced from the travel time in water. All of these travel times are obtained using the equation established by Marczak [27] for the sound speed in water with respect to temperature. The thickness of the liquid phantom is then deduced: $e = L - d_1 - d_2$. When the thickness e is known, the sound speed of the liquid phantom is deduced from the travel-time difference between TR_1 and TR_2 with

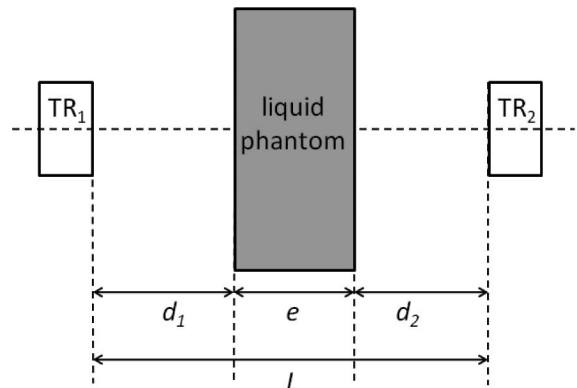


Fig. 3. Schematic diagram of the experiment for characterizing the acoustic properties of liquid phantoms in a flask.

TABLE II. PARAMETERS OF THE LIQUID PHANTOMS AT TEMPERATURE T AND AT A FREQUENCY OF 1 MHz.

Liquid phantom	Thickness e (mm)	Sound speed c (m/s)	Attenuation coefficient α (dB/cm)	Temperature T ($^{\circ}$ C)
Castor oil	35	1523	0.65	22
Rapeseed oil	36	1469	0.07	22
Diethylene glycol	40	1637	0.18	22

and without the flask, and the attenuation coefficient of the liquid phantom is deduced from the ratio of the signal amplitude with and without the flask.

The results for these experiments are given in Table II. The sound speed in castor oil and diethylene glycol is higher than the sound speed in water (1488 m/s at 22° C), whereas the sound speed in rapeseed oil is smaller than this value. Castor oil is the most attenuating liquid phantom of the three. These values of sound speed and attenuation coefficient are in good agreement with those found in the literature [23], [28], [29]. Also, the range of sound speed values using these three liquid phantoms includes the range of sound speeds of the soft tissue layers listed in Table I.

B. Setup for the Pressure Field Measurements

We now describe the setup used to measure the pressure field radiated by a 64-element spherical linear array (Imasonic, Voray-sur-l'Ognon, France). The array's radius of curvature is 110 mm, its width is 92 mm, its height is 30 mm and it operates at a center frequency of 1 MHz. The array is driven by a 256-channel amplifier (IGT, Pessac, France) that is able to send the desired phase law on the elements of the array. The acoustic pressure is measured using a "lipstick" hydrophone and its pre-amplifier (HGL-0200 and AH-2010, Onda Corp., Sunnyvale, CA); the hydrophone is attached to a motion stage controlled by stepper motors in the three spatial directions (MM4006, Newport/Micro-Controle Spectra-Physics S.A., Évry, France).

C. Comparison of the Model Results With Measurements in Water

This set of measurements took place in a tank filled with degassed and deionized water at a temperature of 19° C. Contours of the normalized sound pressure level SPL_{norm} are plotted in Figs. 4 and 5, with $SPL_{\text{norm}} = 20 \log_{10}(|P|/\max|P|)$. In Fig. 4, contours in the plane $y = 0$ and $z = 110$ mm are shown when a constant phase law is applied to the different elements of the array. As a result, the focal point is at the geometric focus: $x_F = 0$ and $z_F = 110$ mm. A very good agreement is observed between the measured and calculated contours of SPL_{norm} at -3 dB and -6 dB. Focal points located 8 cm and 14 cm from the array surface on the acoustic axis are considered in Fig. 5. The measured and calculated contours of SPL_{norm} at -3 dB are very close, whereas the measured contours at -6 dB are slightly larger than the calculated contours. These results show that the model accurately predicts the acoustic field radiated by this type of transducer array in a homogeneous medium.

D. Comparison of the Model Results With Measurements Using Different Liquid Phantoms

For this set of measurements, one of the liquid phantom flasks is placed in front of the spherical linear array, as shown in Fig. 6. The measurements took place in a tank filled with degassed and deionized water, and the temperature was between 22° C and 23° C. The measured and calculated pressure distributions along the acoustic axis

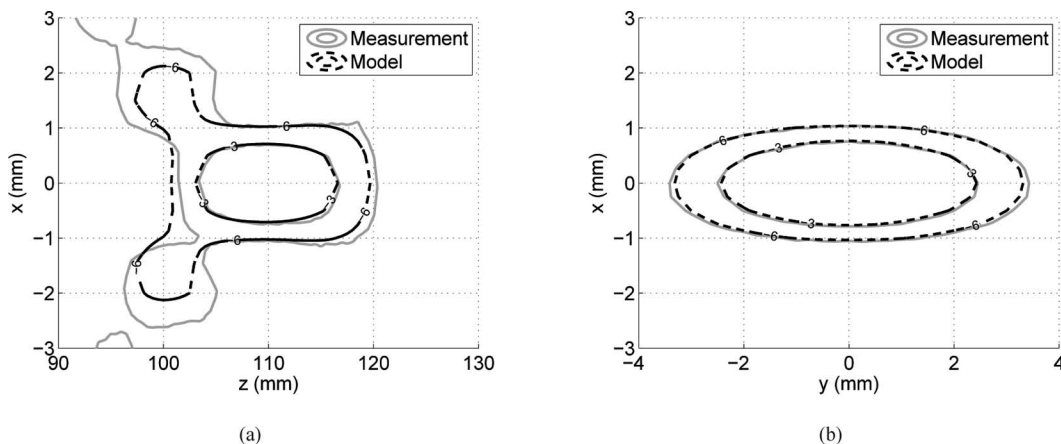


Fig. 4. Contours of the normalized sound pressure levels at -3 dB and at -6 dB for $x_F = 0$ and $z_F = 110$ mm (a) in the plane $y = 0$, and (b) in the plane $z = 110$ mm. The solid gray lines correspond to the measurements and the dashed black lines to the model results.

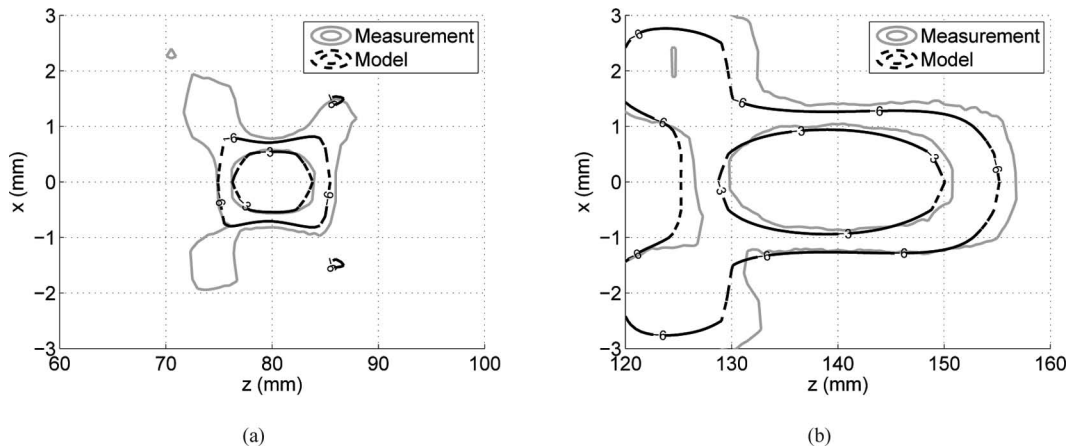


Fig. 5. Contours of the normalized sound pressure levels at -3 dB and at -6 dB in the plane $y = 0$ for $x_F = 0$ and (a) $z_F = 80$ mm, or (b) $z_F = 140$ mm. The solid gray lines correspond to the measurements and the dashed black lines to the model results.

are plotted in Fig. 7 with the focal point at the geometric focus ($x_F = 0$ and $z_F = 110$ mm). For each type of liquid phantom, the pressure distribution is normalized by the maximum value in water and is compared with the pressure distribution in water. The measured focal point is shifted compared with its calculated position. With castor oil and diethylene glycol, the focal point is shifted toward the negative z -axis, whereas with rapeseed oil, the focal point is shifted toward the positive z -axis. This refraction effect is also visible in Fig. 8, where the focal point is at $x_F = 0$ and $z_F = 140$ mm. The measured and calculated maximum peak pressures normalized by their value in water are compared in Table III. These values are in good agreement, with a maximum difference of 3% in all the cases tested.

The shift of the focal point observed in Figs. 7 and 8 can be confirmed by a simple ray-tracing calculation. Rays are sent from different points of the surface of the spherical linear array toward a receiver at (x_R, z_R) , as illustrated in Fig. 9. The rays propagate through water of sound speed c_0 except in the middle layer of thickness e , where they propagate through the liquid phantom of sound speed c_1 . At each interface, the Snell–Descartes law is applied to obtain the transmitted angle. For each point at the array surface, the incident propagation angle of the ray is varied until it reaches the receiver with a given precision (chosen as 0.01 mm). The time of flight of each ray is then straightforwardly obtained. To know the new position of the focal point, we need to find the position of the receiver at which all of the rays arrive in phase (i.e., with the same time of flight). We thus obtain:

- with the castor oil flask: $x_R = 0$ and $z_R = 109.1$ mm;
- with the rapeseed oil flask: $x_R = 0$ and $z_R = 110.6$ mm;
- with the diethylene glycol flask: $x_R = 0$ and $z_R = 105.6$ mm.

It can be seen that the most important shift of the focal point is obtained with the diethylene glycol flask, which is due to the large sound speed difference between diethylene

glycol and water. These focal point positions are represented as dashed vertical lines in Fig. 7; they are close to the maxima of the measured pressure distributions.

In the simulations presented hereafter with the VHP data, the maximum sound speeds are 1615 m/s in skin and 1600 m/s in cartilage, as shown in Table I, which is smaller than the sound speed of diethylene glycol. As a result, these measurements show that the acoustic model is well suited for ultrasound propagation in the body. The peak pressure is well predicted by the model and the error on the focal point position is in the order of a few millimeters.

IV. MODEL RESULTS

A. Choice of the Incident Acoustic Power to Limit Adverse Bioeffects

The choice of the maximum acoustic power that can be sent from the transducer array is guided by safety considerations. To meet the guidance provided by the U.S. Food and Drug Administration [30], the derated spatial-peak temporal-average intensity $I_{SPTA,3}$ should be lower than 720 mW/cm², and the mechanical index (MI) should be lower than 1.9. To meet these criteria, a simulation is first



Fig. 6. Photograph of the setup for the pressure field measurements with a flask filled with a liquid phantom in the path.

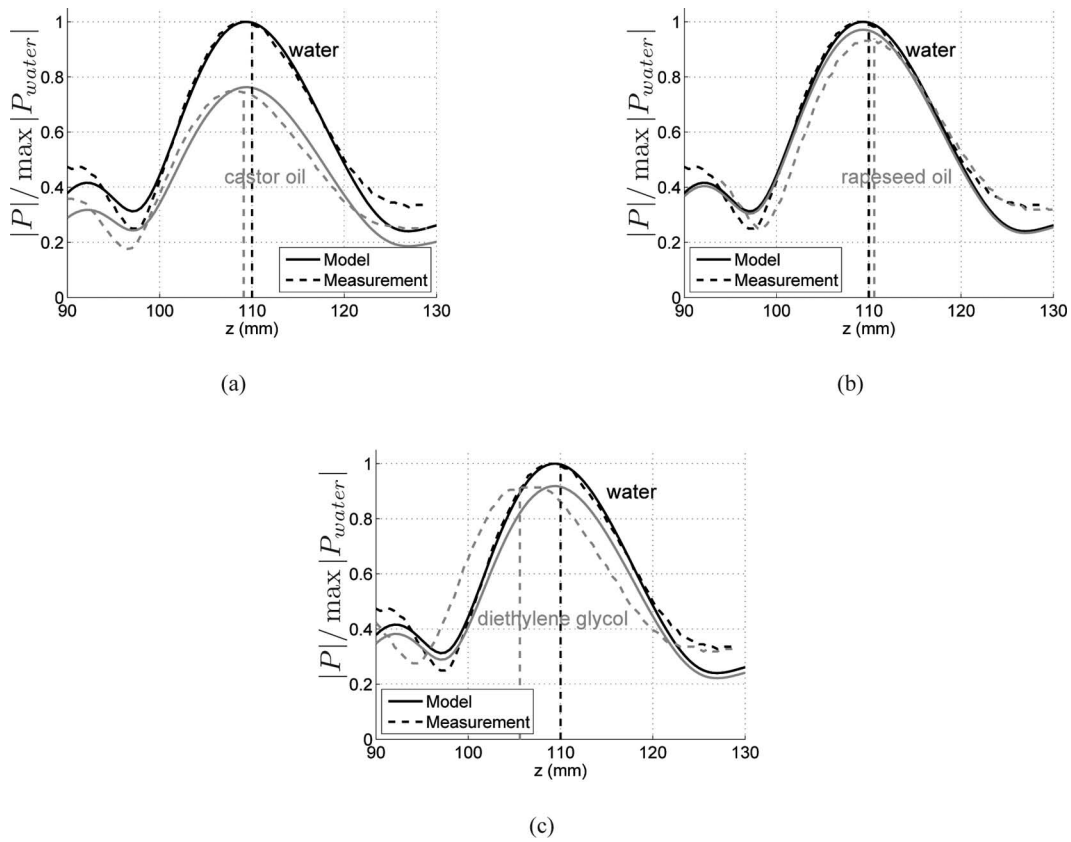


Fig. 7. Pressure distribution along the acoustic axis normalized by its maximum value in water, $\max |P_{\text{water}}|$, for $x_F = 0$ and $z_F = 110$ mm with (a) the castor oil flask, (b) the rapeseed oil flask, and (c) the diethylene glycol flask. The dashed lines correspond to the measurements and the solid lines correspond to the model results; the black lines correspond to the results in water and the gray lines to the results with the liquid flask. The vertical dashed lines correspond to the position of the focal point as predicted by the ray-tracing calculations.

performed in water that yields the pressure field $P(V_n, z)$ for an arbitrary normal velocity $V_n = 1$ m/s. Then, the derated time-average intensity $I_{\text{TA.3}}(V_n, z)$ is calculated using [31]:

$$I_{\text{TA.3}}(V_n, z) = \exp(-0.23 * 0.3 * f_c * z) \frac{|P(V_n, z)|^2}{10^4 \rho_0 c_0} \text{ (W/cm}^2\text{)}, \quad (6)$$

with f_c in megahertz, and z in centimeters. $I_{\text{SPTA.3}}$ is finally found as the spatial maximum of $I_{\text{TA.3}}$, whose location is denoted $z_{m.3}$: $I_{\text{SPTA.3}}(V_n) = I_{\text{TA.3}}(V_n, z_{m.3})$.

The MI is obtained from the derated peak rarefactional pressure $P_{r.3}$ at $z = z_{m.3}$ [31]:

$$\text{MI} = \frac{P_{r.3}(V_n, z_{m.3})}{\sqrt{f_c}}, \quad (7)$$

with f_c in megahertz, and $P_{r.3}$ in megapascals given by

$$P_{r.3}(V_n, z_{m.3}) = \exp(-0.115 * 0.3 * f_c * z) |P(V_n, z_{m.3})|. \quad (8)$$

These expressions relating $I_{\text{SPTA.3}}$ and MI to a given normal velocity V_n are used in Section IV-B to limit the acoustic power sent by the array.

B. Simulation of Ultrasound Propagation

Simulations of ultrasound propagation are performed to estimate the amount of acoustic power received at the target point while meeting the regulations for diagnostic ultrasound devices. The chosen value of $I_{\text{SPTA.3}}$ is equal to the maximum value allowed by FDA regulations, i.e., 720 mW/cm², which corresponds to a mechanical index of 0.15 considering continuous wave signals.

The maps of the attenuation coefficient and of the peak acoustic pressure are plotted in Fig. 10 for both the intercostal and the subcostal paths. The skin is clearly visible as a red line in the attenuation maps, corresponding to a strong attenuation of 3.5 dB/cm. The blocking voxels are plotted in white in these maps. It appears that stomach tissues, and also lung tissues for the intercostal path, hide part of the array from the target point. The acoustic fields are calculated in the domain limited by black lines in the corresponding attenuation maps. The focal region is seen to be elongated along the z -axis and quite narrow along the x -axis. The target point is included in this focal region, which means that a significant amount of power is received at the device position. The peak pressure and time-average intensity are given in Table IV, showing that the results are similar for both acoustic paths. The peak

TABLE III. VALUES OF $\max |P|/\max |P_{\text{water}}|$ MEASURED AND CALCULATED BY THE MODEL FOR THE THREE LIQUID PHANTOMS ($x_F = 0$).

Liquid phantom	$z_F = 110$ mm		$z_F = 140$ mm	
	Measured (%)	Calculated (%)	Measured (%)	Calculated (%)
Castor oil	75	76	75	77
Rapeseed oil	94	97	98	97
Diethylene glycol	91	92	95	92

pressure at the target point is close to the maximum peak pressure in the whole field; for example, the maximum peak pressure is 63 kPa for the subcostal path compared with a value of 58 kPa at the target point.

The calculations are quite intensive because of the large number of elements needed to discretize the array surface [$M = 38784$ in the summation of (4)] and of the large propagation distances. Indeed, for each contribution from a surface element to a field point, an interpolation is performed to identify the tissue layers crossed, which is time-consuming. The calculations presented here take about 10 h to run on a personal computer equipped with 8 GB of RAM memory, distributing the calculations between two cores of a processor running at 3.0 GHz.

C. Prediction of Temperature Rise in Tissues

Calculations of the temperature rise in tissues resulting from ultrasound propagation are now performed to check that thermal effects are small with the incident acoustic

power chosen in Section IV-A. First, the acoustic pressure field is calculated in a volume using the model described in Section II-B. Second, the temperature field is obtained in a larger volume using the model described in Section II-C. The choice of two different computation domains for the acoustic and thermal calculations comes from the fact that the acoustic model is time-consuming, and thus the acoustic calculation must be limited to the domain where most of the energy is contained. On another hand, the thermal model runs rapidly (of the order of a few minutes), despite the importance of requiring a large enough domain to avoid any boundary effects. The two different computation domains are shown in Fig. 11 for the intercostal path.

In these thermal simulations, ultrasound waves are sent continuously for 30 min. Then, the calculation runs for 10 min more to observe the cooling period. Results are presented for the intercostal path in Figs. 12 and 13. First, in Fig. 12, the acoustic intensity fields in the planes $y = 0$ and $x = 30$ mm are plotted for the intercostal path. It

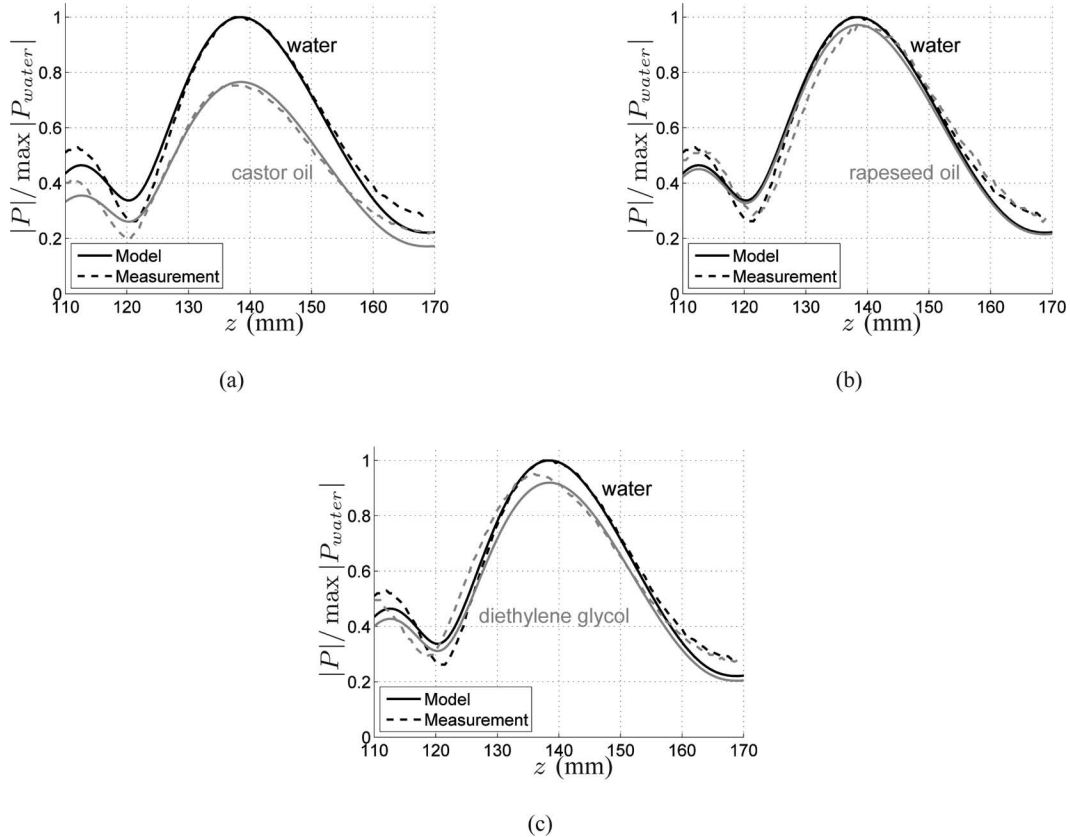


Fig. 8. The same as Fig. 7, but with $x_F = 0$ and $z_F = 140$ mm.

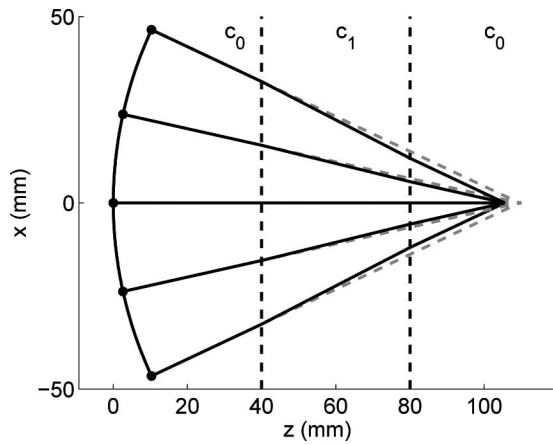


Fig. 9. Rays from different points of the surface of the spherical linear array propagating through the diethylene glycol flask ($e = 40$ mm, $c_0 = 1491$ m/s, and $c_1 = 1637$ m/s) and arriving in phase at a receiver at $x = 0$ and $z = 105.6$ mm.

can be seen that the focal zone, where most of the acoustic energy is sent, is narrow along the x -axis and wider over the y -axis because of the geometry of the array. The local deposited heat Q is proportional to the acoustic intensity, as explained in Section II-C. The fields of the temperature rise after 30 min are presented in Fig. 13. The shape of the heated zone is similar to the shape of the focal zone. The temperature rise is small, less than 0.3°C for all the points of the field.

The evolution of the temperature rise with time at the target point is shown in Fig. 14 for both the intercostal and subcostal paths. The temperature increases up to its maximum value after a few minutes and remains constant until 30 min. For the remaining 10 min, there is no deposited heat due to ultrasound [$Q = 0$ in (5)] and the temperature goes rapidly back to its initial value. The maximum temperature reached in the subcostal case is almost the same as in the intercostal case.

V. DISCUSSION

The calculations performed in this study show that deeply implanted devices can potentially be empowered by ultrasonic waves without causing significant temperature rise or cavitation in tissues. The device considered is implanted in the abdomen, approximately 15 cm from the skin. For the two acoustic paths considered, a time-average intensity greater than 0.1 W/cm^2 is reached at the target point. However, this relatively high acoustic power is obtained in a small spatial domain, especially over the x -axis, where the -6-dB beamwidth is between 3 and 4 mm. This means that the position of the device must be known with a good precision. Also, the device position will be subjected to breathing motion, which can be as large as 20 mm for some organs [32]. Thus, a precise tracking of the device might be needed for the acoustic powering to be efficient. This topic is outside the scope of this paper and will be dealt with in future papers. It should also be

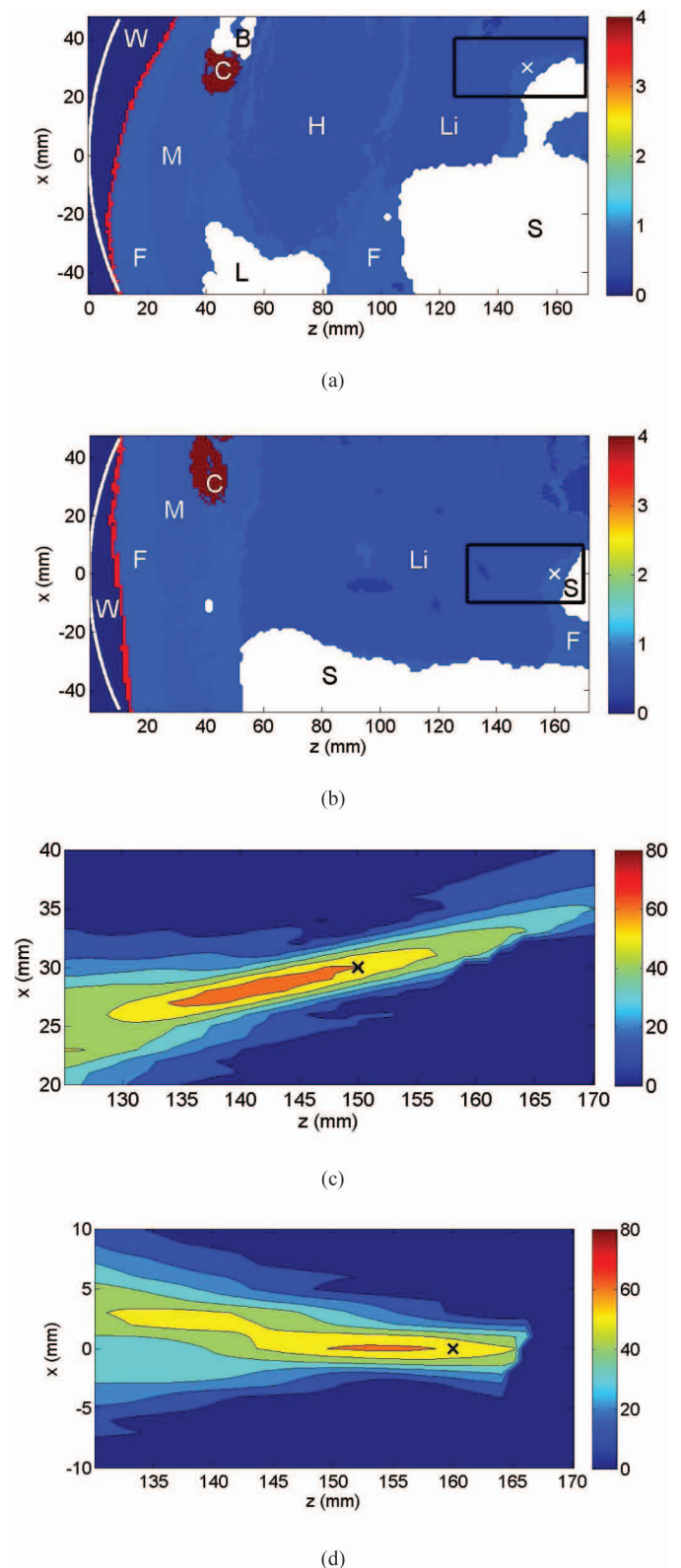


Fig. 10. Maps of the attenuation coefficient in decibel per centimeter for (a) the intercostal path and (b) the subcostal path, and maps of the peak acoustic pressure in kilopascals for (c) the intercostal path and (d) the subcostal path. The pressure fields are calculated in the black box plotted in the corresponding attenuation map. The crosses correspond to the target point. In the maps of the attenuation coefficient, the transducer array and the blocking voxels are represented in white.

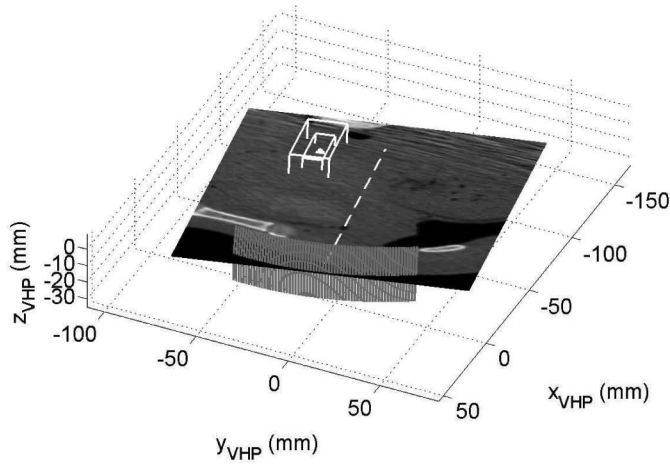


Fig. 11. Frozen computed tomography scan for the intercostal path with the limits of the computation domains for the acoustic calculation (small volume) and for the temperature calculation (large volume) represented as solid white lines. The dot corresponds to the target point, and the dashed line to the acoustic axis of the array.

emphasized that only one body geometry, from the Visible Human Male, has been considered. It would be interesting to study the variability of body geometry among individuals and its effect on acoustic powering efficiency in future studies.

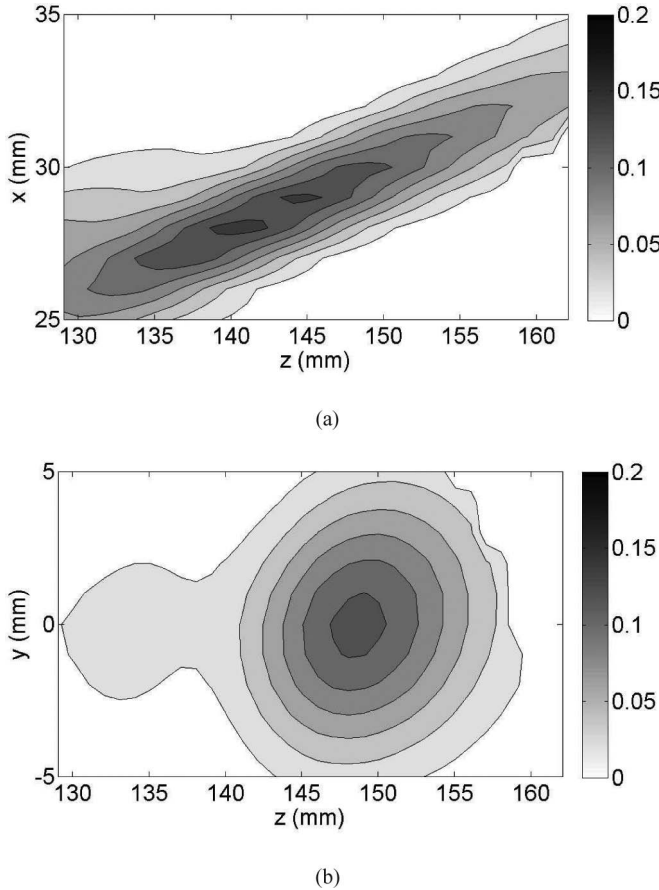


Fig. 12. Maps of the time-average acoustic intensity in watt per centimeter squared for the intercostal path (a) in the horizontal plane $y = 0$, and (b) in the vertical plane $x = 30$ mm.

TABLE IV. RESULTS OF THE ACOUSTIC CALCULATIONS FOR THE TWO ACOUSTIC PATHS.

	V_n (mm/s)	$ P $ at target (kPa)	I_{TA} at target (mW/cm ²)
Intercostal path	14.8	60	123
Subcostal path	15.2	58	115

The results validate the choice of an ultrasonic frequency around 1 MHz. A good penetration depth is indeed obtained at this frequency and beamforming has been shown to be efficient. It could be beneficial to use a two-dimensional array to facilitate the alignment of the acoustic beam with the device. Also, a reduction of the external transducer in size would be desirable. A smaller transducer would be easier to handle and a smaller extent of blocking tissues would be encountered.

The acoustic model considers the heterogeneous attenuation in the different tissue layers, but does not account for refraction and reflection effects because it would be too complicated to implement in a realistic environment. The comparison with measurements in heterogeneous phantoms shows that the measured focal point can be slightly shifted compared with the calculated one, even though the shift remains smaller than 4 mm for soft tissue layers. The calculated peak pressures agree well with the measurement results.

An important assumption made in the model is that other tissues such as bones, lungs, and stomach are block-

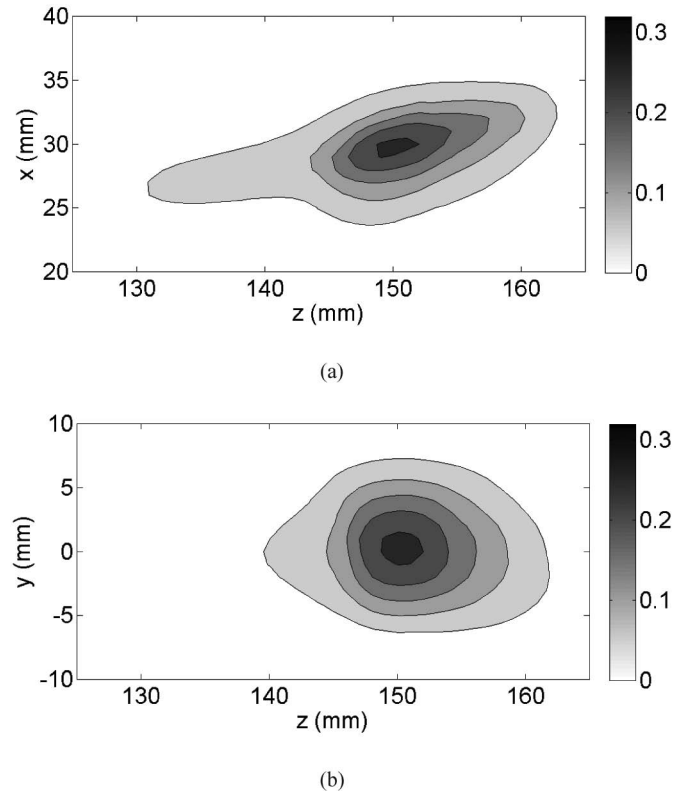


Fig. 13. Maps of the temperature rise in degrees Celsius after 30 min for the intercostal path (a) in the horizontal plane $y = 0$, and (b) in the vertical plane $x = 30$ mm.

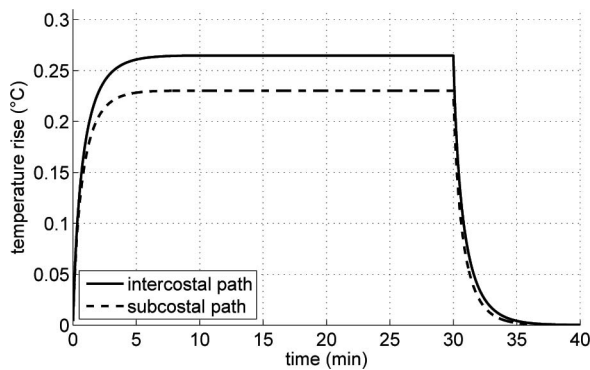


Fig. 14. Temperature rise in degrees Celsius with respect to time for the intercostal and subcostal paths at their target point ($x = 30$ mm, $y = 0$, and $z = 150$ mm for the intercostal path, $x = y = 0$ and $z = 160$ mm for the subcostal path).

ing ultrasound propagation. Because of the large size of the transducer array, it is not possible to completely avoid ultrasound wave propagation through these organs. The blocking voxel assumption is discussed in detail in Pichardo and Hynynen [15]. This assumption can yield to an underestimation of thermal effects. Because the acoustic power radiated by the array is limited following FDA regulations, with which echographic and other diagnostic devices must comply, it is very unlikely that significant heating could occur in bones, lungs, or stomach tissue. This should nevertheless be tested in an *in vivo* environment.

There exist other linear models that have been used for ultrasound 3-D propagation in tissue-like media. One can cite mainly the models based on a finite-difference time-domain (FDTD) solution of the wave equation in heterogeneous absorbing media, such as the one used by Marquet *et al.* [33] for ultrasound propagation through the human skull, and the models based on the boundary element method (BEM), such as the one used by Gélat *et al.* [34] for acoustic wave scattering by human ribs. The FDTD method accurately models attenuation, refraction, and reflection effects that occur in tissues modeled as fluid media; however mode conversions and shear waves are not taken into account. The entire 3-D domain must be discretized, thus requiring considerable computational time and memory for realistic configurations. Also, it is more adapted to pulse wave excitation because it is a time-domain method. The BEM model proposed by Gélat *et al.* [34] is powerful for predicting the acoustic field scattered by ribs, modeled as perfectly rigid boundaries. It is based on the Helmholtz integral equation, which involves an integral over the scattering surface, and assumes that the fluid medium surrounding the scatterer is homogeneous and non-dissipative. Thus, only a 2-D mesh is needed to model 3-D propagation. However, attenuation, refraction, and reflection effects are not accounted for. This brief comparison shows that FDTD and BEM models possess some advantages compared with the model based on the Rayleigh–Sommerfeld diffraction integral. They are however more computationally intensive, typically requiring hours of calculation over a cluster computer; for instance the calculations are distributed over 100 cluster cores in [34].

Finally, it can be noted that different researchers have studied the influence of ribs on the ultrasonic and thermal fields in the context of thermal ablation by ultrasound [35], [36]. In these applications, ultrasound pressure is much stronger and nonlinear effects can become significant. In this case, nonlinear propagation models such as the one used by Li *et al.* [35] could be considered. It must be noted, however, that different studies continue to use linear propagation models in this context [33], [34], [36]. In the present study, in which the goal is to transfer energy to implanted devices, we can safely assume linear acoustic propagation because the pressure levels radiated by the array are relatively low to comply with FDA regulations and because of the relatively low ultrasound frequency.

VI. CONCLUSION

This theoretical study shows that a safe and efficient energy transfer can be obtained between a transducer array located externally on the patient’s skin and a device deeply implanted in the abdomen. Two suitable acoustic paths have been found using the Visible Human Project data and simulations of ultrasound propagation have been performed considering this geometry. The acoustic model has been validated experimentally in water and in heterogeneous media made with liquid phantoms. By limiting the acoustic power radiated by the array following safety guidelines, we showed that acoustic intensity greater than 0.1 W/cm² was obtained at the device position while minimizing adverse bioeffects. Predictions of the temperature rise in tissue resulting from ultrasound propagation confirm that thermal effects are small.

ACKNOWLEDGMENTS

The authors acknowledge the National Library of Medicine (NLM) and the Visible Human Project as the source of the data used in this study.

REFERENCES

- [1] C. Edman and D. Drinan, “A review of the management of implanted medical devices for diabetes: Trends and directions,” *J. Diabetes Sci. Technol.*, vol. 2, no. 6, pp. 995–1002, 2008.
- [2] Y. Yun, Z. Dong, N. Lee, Y. J. Liu, D. C. Xue, X. F. Guo, J. Kuhlmann, A. Doepke, H. B. Halsall, W. Heineman, S. Sundaramurthy, M. J. Schulz, Z. Z. Yin, V. Shanov, D. Hurd, P. Nagy, W. F. Li, and C. Fox, “Revolutionizing biodegradable metals,” *Mater. Today*, vol. 12, no. 10, pp. 22–32, 2009.
- [3] A. Hasan and V. Paul, “Telemonitoring in chronic heart failure,” *Eur. Heart J.*, vol. 32, no. 12, pp. 1457–1464, 2011.
- [4] C. Stahl, T. Walker, A. Straub, K. Kettering, K. Knubben, T. O. Greiner, S. Paule, M. Lippert, G. Czygan, O. Schweika, and V. Kuhlkamp, “Assessing acute ventricular volume changes by intracardiac impedance in a chronic heart failure animal model,” *Pacing Clin. Electrophysiol.*, vol. 32, no. 11, pp. 1395–1401, 2009.
- [5] T. Maleki, N. Cao, S. H. Song, C. Kao, S. C. Ko, and B. Ziaie, “An ultrasonically powered implantable micro-oxygen generator (IMOG),” *IEEE Trans. Biomed. Eng.*, vol. 58, no. 11, pp. 3104–3111, 2011.

- [6] J. Lueke and W. A. Moussa, "MEMS-based power generation techniques for implantable biosensing applications," *Sensors*, vol. 11, no. 2, pp. 1433–1460, 2011.
- [7] G. Vandevoorde and R. Puers, "Wireless energy transfer for stand-alone systems: A comparison between low and high power applicability," *Sens. Actuators*, vol. A92, no. 1–3, pp. 305–311, 2001.
- [8] M. Sawan, S. Hashemi, M. Sehil, F. Awwad, M. Hajj-Hassan, and A. Khouas, "Multicoils-based inductive links dedicated to power up implantable medical devices: Modeling, design, and experimental results," *Biomed. Microdevices*, vol. 11, no. 5, pp. 1059–1070, 2009.
- [9] A. Denisov and E. Yeatman, "Ultrasonic vs. inductive power delivery for miniature biomedical implants," in *Proc. Int. Conf. Body Sensor Networks*, 2010, pp. 84–89.
- [10] S. Ozeri and D. Shmilovitz, "Ultrasonic transcutaneous energy transfer for powering implanted devices," *Ultrasonics*, vol. 50, no. 6, pp. 556–566, 2010.
- [11] A. Penner, "Acoustically powered implantable stimulating device," U.S. Patent 0172083, Sep. 2, 2004.
- [12] N. P. Willis, A. F. Briskin, M. W. Cowan, M. Pare, R. Fowler, and J. Brennan, "Optimizing energy transmission in a leadless tissue stimulating system," U.S. Patent 0294208, Nov. 27, 2008.
- [13] B. C. Tran, B. Min, and R. S. Harguth, "Systems and methods for controlling wireless signal transfers between ultrasound-enabled medical devices," U.S. Patent 0201148, Aug. 13, 2009.
- [14] S. Ozeri, D. Shmilovitz, S. Singer, and C.-C. Wang, "Ultrasonic transcutaneous energy transfer using a continuous wave 650 kHz Gaussian shaded transmitter," *Ultrasonics*, vol. 50, no. 7, pp. 666–674, 2010.
- [15] S. Pichardo and K. Hynynen, "Circumferential lesion formation around the pulmonary veins in the left atrium with focused ultrasound using a 2D-array endoesophageal device: A numerical study," *Phys. Med. Biol.*, vol. 52, no. 16, pp. 4923–4942, 2007.
- [16] H. T. O'Neil, "Theory of focusing radiators," *J. Acoust. Soc. Am.*, vol. 21, no. 5, pp. 516–526, 1949.
- [17] X. Fan and K. Hynynen, "The effects of curved tissue layers on the power deposition patterns of therapeutic ultrasound beams," *Med. Phys.*, vol. 21, no. 1, pp. 25–34, 1994.
- [18] E. G. Moros, X. Fan, and W. L. Straube, "Ultrasound power deposition model for the chest wall," *Ultrasound Med. Biol.*, vol. 25, no. 8, pp. 1275–1287, 1999.
- [19] H. H. Pennes, "Analysis of tissue and arterial blood temperatures in the resting human forearm," *J. Appl. Physiol.*, vol. 1, no. 2, pp. 93–122, 1948.
- [20] J. C. Chato, "Fundamentals of bioheat transfer," in *Thermal Dosimetry and Treatment Planning*, M. Gautherie, Ed., Heidelberg, Germany: Springer-Verlag, 1990, pp. 1–56.
- [21] F. Chavrier, J.-Y. Chapelon, A. Gelet, and D. Cathignol, "Modeling of high-intensity focused ultrasound-induced lesions in the presence of cavitation bubbles," *J. Acoust. Soc. Am.*, vol. 108, no. 1, pp. 432–440, 2000.
- [22] ICRU, *Tissue Substitutes, Phantoms and Computational Modeling in Medical Ultrasound*, International Commission on Radiation Units and Measurements, Bethesda, MD, Report 61, 1998.
- [23] F. A. Duck, *Physical Properties of Tissue: A Comprehensive Reference Book*, London, UK: Academic Press, 1990.
- [24] ESHOTGR, "Treatment planning and modelling in hyperthermia," in *Tor Vergata Medical Physics Monograph Series*, European Society for Hyperthermic Oncology Task Group Report, University of Rome, Rome, 1992.
- [25] H. J. Nieminen, S. Saarakkala, M. S. Laasanen, J. Hirvonen, J. S. Jurvelin, and J. Töyräs, "Ultrasound attenuation in normal and spontaneously degenerated articular cartilage," *Ultrasound Med. Biol.*, vol. 30, no. 4, pp. 493–500, 2004.
- [26] G. Kossoff, E. K. Fry, and J. Jellins, "Average velocity of ultrasound in the human female breast," *J. Acoust. Soc. Am.*, vol. 53, no. 6, pp. 1730–1736, 1973.
- [27] W. Marczak, "Water as a standard in the measurements of speed of sound in liquids," *J. Acoust. Soc. Am.*, vol. 102, no. 5, pp. 2776–2779, 1997.
- [28] A. Selfridge, "Approximate material properties in isotropic materials," *IEEE Trans. Sonics Ultrason.*, vol. SU-32, no. 3, pp. 381–394, 1985.
- [29] B. E. Treeby, B. T. Cox, E. Z. Zhang, S. K. Patch, and P. C. Beard, "Measurement of broadband temperature-dependent ultrasonic attenuation and dispersion using photoacoustics," *IEEE Trans. Ultrason. Ferroelectr. Freq. Control*, vol. 56, no. 8, pp. 1666–1676, 2009.
- [30] FDA, "Information for manufacturers seeking clearance of diagnostic ultrasound systems and transducers," U.S. Food and Drug Administration, Center for Devices and Radiological Health, Rockville, MD, 2008.
- [31] AIUM/NEMA, "Acoustic output measurement standard for diagnostic ultrasound equipment," American Institute of Ultrasound in Medicine, Laurel, MD, National Electrical Manufacturers Association, Rosslyn, VA, Revision 1, 2004.
- [32] M. Pernot, M. Tanter, and M. Fink, "3-D real-time motion correction in high-intensity focused ultrasound therapy," *Ultrasound Med. Biol.*, vol. 30, no. 9, pp. 1239–1249, 2004.
- [33] F. Marquet, M. Pernot, J.-F. Aubry, G. Montaldo, L. Marsac, M. Tanter, and M. Fink, "Non-invasive transcranial ultrasound therapy based on a 3D CT scan: Protocol validation and *in vitro* results," *Phys. Med. Biol.*, vol. 54, no. 9, pp. 2597–2613, 2009.
- [34] P. Gélât, F. ter Haar, and N. Saffari, "Modelling of the acoustic field of a multi-element HIFU array scattered by human ribs," *Phys. Med. Biol.*, vol. 56, no. 17, pp. 5553–5581, 2011.
- [35] J.-L. Li, X.-Z. Liu, D. Zhang, and X.-F. Gong, "Influence of ribs on the nonlinear sound field of therapeutic ultrasound," *Ultrasound Med. Biol.*, vol. 33, no. 9, pp. 1413–1420, 2007.
- [36] S. Bobkova, L. Gavrilov, V. Khokhlova, A. Shaw, and J. Hand, "Focusing of high-intensity ultrasound through the rib cage using a therapeutic random phased array," *Ultrasound Med. Biol.*, vol. 36, no. 6, pp. 888–906, 2010.



Benjamin Cotté received his M.S. degree in acoustics from Penn State University in 2005 and his Ph.D. degree in acoustics from École Centrale de Lyon in 2008, where he studied acoustic wave propagation in the atmosphere in the context of high speed trains.

He joined the INSERM U556 in 2009 as a postdoctoral researcher, where he worked on energy transfer by ultrasound for medical applications and ultrasound wave propagation in tissues. Since 2011, he has been an Assistant Professor at the École Nationale Supérieure des Techniques Avancées (ENSTA) in Paris, France. His current research interests include acoustic propagation in inhomogeneous media and time-domain modeling in structural acoustics.

Dr. Benjamin Cotté is a member of the Acoustical Society of America and of the Société Française d'Acoustique.



Cyril Lafon was born in Saint Yrieix la Perche, France, in 1974. He received the B.Sc. degree in physics from the University Blaise Pascal, Clermont-Ferrand, France, including studying abroad at the University of Montreal, Montreal, QC, Canada, in 1995, and the Ph.D. degree in biomedical engineering from the University Claude Bernard Lyon 1, Lyon, France, in 1999.

For two years, he was a Postdoctoral Research Fellow in the Applied Physics Laboratory, University of Washington, Seattle, where he was engaged in ultrasound-induced hemostasis and the development of tissue-mimicking phantoms for high-intensity focused ultrasound (HIFU) applications. Since 2002, he has been a Research Scientist at the Institut National de la Santé et de la Recherche Médicale (INSERM), Laboratory on Therapeutic Applications of Ultrasound, Lyon, France. His current research interests include modeling ultrasound wave propagation, development of ultrasonic therapeutic devices for thermal ablation or drug delivery, and communication by ultrasound for medical applications.

Dr. Cyril Lafon has been a member of IEEE since 2002.



Catherine Dehollain (M'93) received the degree in electrical engineering in 1982 and the Ph.D. degree in 1995 from the Ecole Polytechnique Fédérale de Lausanne (EPFL), Lausanne, Switzerland.

From 1982 to 1984, she was a Research Assistant at the Electronics Laboratories (LEG), EPFL. In 1984, she joined the Motorola European Center for Research and Development, Geneva, Switzerland, where she designed integrated circuits for telecommunications applications. In

1990, she joined EPFL as a Senior Assistant at the Chaire des Circuits et Systèmes, where she was involved in broadband impedance matching. Since 1995, she has been responsible for the RFIC Group, EPFL, for RF activities. She has been the technical project manager of the European projects, CTI projects, and the Swiss National Science Foundation projects dedicated to RF wireless micropower sensor networks and mobile phones. Since 1998, she has been a Lecturer at EPFL in the area of RF circuits, electric filters, and CAD tools. Since 2006, she has been a Maître d'Enseignement et de Recherche at EPFL. She is an author or co-author of four scientific books and 75 scientific publications. Her current research interests include low-power analog circuits, biomedical remotely powered sensors, and electrical filters.



Jean-Yves Chapelon was born in France on April 9, 1953. He holds an M.S. degree from the University Jean Monet, Saint-Etienne, and a Ph.D. degree in biomedical engineering from the University of Lyon 1. Since 1978, he has been with the National Institut for Health and Medical Research (INSERM), where he is presently Director of Research.

Dr. Chapelon is Director of the laboratory LabTAU (Laboratory of Therapeutic Applications of Ultrasound), INSERM U1032, fully affiliated with the University of Lyon 1. His current research interests are in

high-intensity focused ultrasound (HIFU): designing clinical prototype devices, developing methods of monitoring HIFU treatments, and studying the biology and biophysics involved in the treatments.

Dr. Chapelon is currently a fellow of the Acoustical Society of America and a member of the IEEE UFFC Society, IEEE EMB Society, the European Society for Hyperthermic Oncology, the International Society on Therapeutic Ultrasound, the Société Française de Génie Biologique et Médical, and the Société Française d'Acoustique.